Research Article

Improving the band alignment at PtSe$_2$ grain boundaries with selective adsorption of TCNQ

Yanhui Hou[1,§], Ziqiang Xu[1,§], Yan Shao[2], Linlu Wu[3], Zhongliu Liu[2], Genyu Hu[1], Wei Ji[3], Jingsi Qiao[1] (✉),
Xu Wu[1] (✉), Hong-Jun Gao[2], and Yeliang Wang[1] (✉)

[1] MIIT Key Laboratory for Low-Dimensional Quantum Structure and Devices, School of Integrated Circuits and Electronics, Beijing Institute of Technology, Beijing 100081, China
[2] Institute of Physics, Chinese Academy of Sciences, Beijing 100190, China
[3] Department of Physics and Beijing Key Laboratory of Optoelectronic Functional Materials and Micro-nano Devices, Renmin University of China, Beijing 100872, China
[§] Yanhui Hou and Ziqiang Xu contributed equally to this work.

ABSTRACT

Grain boundaries in two-dimensional (2D) semiconductors generally induce distorted band alignment and interfacial charge, which impair their electronic properties for device applications. Here, we report the improvement of band alignment at the grain boundaries of PtSe$_2$, a 2D semiconductor, with selective adsorption of a presentative organic acceptor, tetracyanoquinodimethane (TCNQ). TCNQ molecules show selective adsorption at the PtSe$_2$ grain boundary with strong interfacial charge. The adsorption of TCNQ distinctly improves the band alignment at the PtSe$_2$ grain boundaries. With the charge transfer between the grain boundary and TCNQ, the local charge is inhibited, and the band bending at the grain boundary is suppressed, as revealed by the scanning tunneling microscopy and spectroscopy (STM/S) results. Our finding provides an effective method for the advancement of the band alignment at the grain boundary by functional molecules, improving the electronic properties of 2D semiconductors for their future applications.

KEYWORDS

organic-two-dimensional (2D) heterostructure, PtSe$_2$, grain boundary, band alignment, scanning tunneling microscopy (STM)

1   Introduction

Two-dimensional (2D) transition metal dichalcogenides (TMDs) are promising in future device applications with excellent electronic and optoelectronic properties [1–9]. As the common one-dimensional (1D) defect structure, grain boundaries (GBs) can adversely affect the electronic properties of 2D TMDs by inducing band bending and interfacial charge, which often impairs the device performance of 2D-based semiconductors [10–13]. Thus, it is essential to find a way to suppress the effect of the GBs on the device performance. Although the improved fabrication method can decrease the GBs density and promote the properties of 2D TMDs, some GBs still inevitably exist during the synthesis and thermal treatment, due to the marginal energy of forming GBs [14–19]. Tuning the electronic properties at the boundaries is another way of attenuating the effects of GBs. Recently, the electronic properties of GBs in TMDs, such as band alignment, have been intensively studied [13, 20–24]. However, unlike the characterization study, the work for precisely tuning the band alignment of the GBs is still rare, though this will bring a substantial benefit in improving the properties of 2D TMDs.

Combined with the flexibility of organic molecules and the template effect of 2D materials, the organic-2D heterostructure offers a promising platform for tuning the local electronic properties of 2D TMDs [25–28]. In particular, the nanostructures in 2D TMDs always show a template effect on the adsorbed molecules and induce site-specific adsorbed structures, such as selective self-assembly and adsorptions [29–31]. As a representative example of 2D TMDs, the PtSe$_2$ suffers from the effects of GBs in device applications, due to the difficulty in large-scale fabrication, despite its excellent electronic properties, such as high mobilities and wide band gap [32–37]. In light of the reported selective adsorption of PtSe$_2$ [29], organic-2D heterostructure may offer a promising opportunity for precisely tuning the properties of the PtSe$_2$ GBs, thus, improving its performance in the electronic devices.

Here, we reported the study of tuning of band alignment at the GBs in monolayer PtSe$_2$ with selective absorption of the organic acceptor, tetracyanoquinodimethane (TCNQ). Using scanning tunneling microscopy and spectroscopy (STM/S), we investigate the structure and band alignment of GBs in monolayer PtSe$_2$ in atomic scale. The results reveal two different band alignment features, which indicate the distinct interfacial charge at the GBs. TCNQ has selective adsorption at the preferred GBs with a stronger interfacial charge. Due to the charge transfer between the organic acceptor and GBs, the interfacial charge is weakened at the

boundary with adsorption, which is indicated by an inhibited band bending in the STS results. Our findings demonstrate the ability of organic-2D heterostructure to improve the band alignment at the GBs. Reducing the adverse effect of the GBs, our study provides an effective method for improving the electronic properties of 2D semiconductors for their future applications.

2   Experimental

2.1   Sample preparation

Monolayer $PtSe_2$ was fabricated by direct selenization of Pt(111) in an ultrahigh vacuum chamber, with a base pressure of 2×10^{-10} mbar, equipped with standard molecular beam epitaxy (MBE) capabilities. The Pt(111) substrate was cleaned by several cycles of Ar^+ ion sputtering followed by annealing at 700 K, and clean surface terraces in the STM images were obtained. High-purity Se and TCNQ evaporated from Knudsen cells were deposited onto the samples, which were kept at 520 K for selenization and 80 K for selective adsorption, respectively. After growth, the sample was transferred to an STM chamber for measurement.

2.2   Scanning tunneling microscopy measurements

To obtain the electronic properties of the films, STM experiments were performed using a low-temperature STM system that was operated at a base temperature of 4.5 K. Electrochemically etched tungsten tips were cleaned *in situ* using electron beam bombardment. The differential conductance (dI/dV) was measured using lock-in detection of the tunnel current (I) by adding 5 mV modulated bias voltage at 973 Hz to the sample bias voltage (V). All the STM images were measured in constant current mode.

3   Results and discussion

The monolayer $PtSe_2$ samples were fabricated on the Pt(111) substrate by directly selenization of Pt in the ultrahigh-vacuum (UHV) system [32]. Figure 1(a) shows a typical STM topography image of the monolayer $PtSe_2$ on Pt(111). Instead of a flat surface, two main grains of $PtSe_2$ with different apparent heights can be observed, and named the lower layer (LL) and the higher layer (UL) as labeled. The lattice in the STM image is the typical $PtSe_2(3 \times 3)/Pt(4 \times 4)$ moiré pattern, which originates from the lattice mismatch between the $PtSe_2$ and Pt substrate (for more details see Fig. S1 in the Electronic Supplementary Material (ESM)). As shown in Figs. 1(b) and 1(c), both UL and LL own the same moiré pattern, indicating the same monolayer thickness and Pt(111) substrate underneath. The corresponding line profiles reveal the height difference between LL and UL is around 2.3 Å, which is equal to the height of the Pt(111) step.

Considering the same monolayer thickness and height difference of one Pt(111) step, the formation of the LL and UL grains can be attributed to the lattice mismatch between $PtSe_2$ and Pt(111) substrate. During the fabrication, the Pt atoms in the top layer on the substrate cannot be totally selenized, since the density of Pt atom in the top layer is higher than that of the formed $PtSe_2$. Then a portion of Pt atoms forms an additional substrate layer underneath the grown monolayer $PtSe_2$, generating the UL. Simultaneously, the GBs are appeared in between the LL and UL. Combined with the STM simulation and the moiré pattern features (for more details see Figs. S2 and S3 in the ESM) [32], the lattice orientation of $PtSe_2$ on the Pt(111) substrate can be confirmed. Thus, the structures of the GBs can be depicted as shown in Figs. 1(d)–1(f) (for more details see Fig. S4 in the ESM). Due to the $P\bar{3}m1$ space group of $PtSe_2$, there are two types of GBs
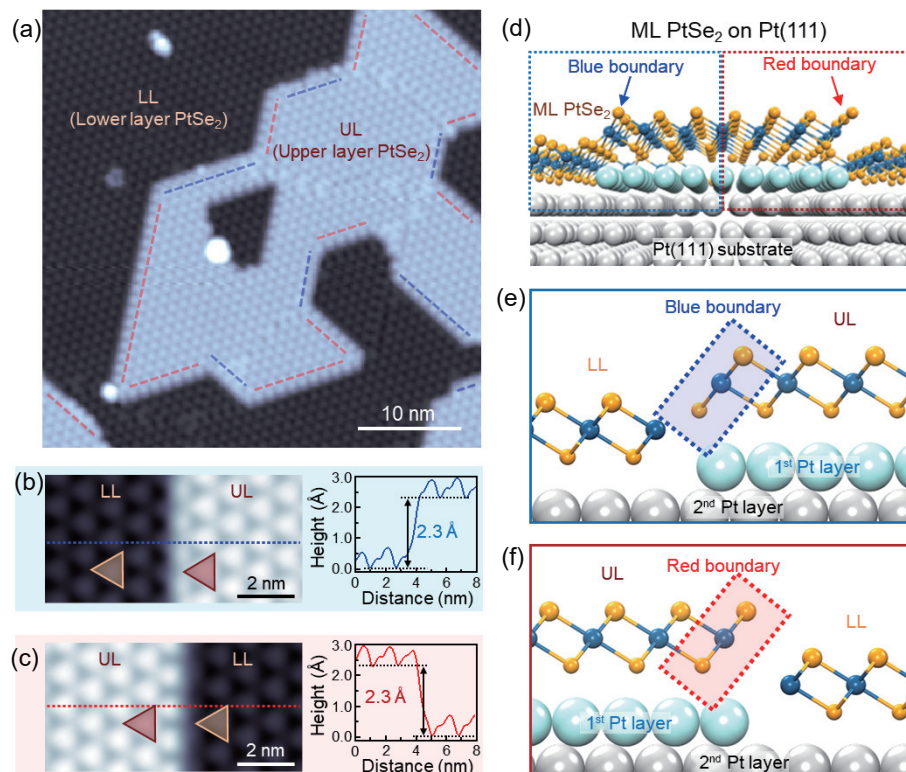

Figure 1 (a) STM image of the monolayer $PtSe_2$ with UL and LL grains. (b) and (c) Zoom-in STM images of the grain boundaries of monolayer $PtSe_2$. The blue and red curves are the corresponding line profiles along with the blue and red dotted lines in the STM images, respectively. The orientations of the moiré superlattice on UL and LL are depicted by red and pink triangles, respectively. (d) Schematic model of the grain boundaries of monolayer $PtSe_2$. The two types of grain boundaries are marked by blue and red lines. (e) and (f) The zoom-in schematic model of the two types of grain boundaries ((e) blue boundary and (f) red boundary) from the side view. The grain boundaries are marked by blue and red dotted rectangles. The blue (light blue and grey) and orange spheres represent Pt and Se atoms in $PtSe_2$, respectively. The Pt spheres with different colors and sizes are used to differentiate the Pt atoms in the Pt(111) substrate and $PtSe_2$. STM scanning parameters: (a) sample bias: $U = -2.0$ V, setpoint: $I = 10$ pA; (left panels of (b) and (c)) $U = -1.0$ V, setpoint: $I = 50$ pA.

with opposite orientations and different atomic configurations, named blue boundary and red boundary as labeled.

In order to characterize the band alignment at the blue boundary and red boundary, we performed STS constant-height dI/dV spectra to measure the local density of states (DOS), across the typical GBs in Figs. 2(a) and 2(e). Figures 2(b) and 2(f) are the dI/dV STS linescans taken along the blue and red dashed arrows in Figs. 2(a) and 2(e), respectively. The results reveal the unambiguous distinction between the band alignment at the blue boundary and red boundary. In the linescan results, interruptions of the band features appear at the edges, indicating the discontinuous band alignment across the GBs. In addition, we can see the band bending of each GB, with the characteristic DOS peak in the conductance band (CB). The outline of the valence band (VB) can still be roughly recognized, although the features are a little dim. To present the results concisely, the schematic diagrams of band alignment at the blue and red boundary, based on the linescan mappings, are shown in Figs. 2(c) and 2(g). On the LL side, the band bending is negligible for both the blue and red boundaries. On the UL side, a slight upward band bending was observed at the blue boundary. In contrast, a significantly upward band bending can be detected at the red boundary.

To investigate the band bending in detail, we further slice the mapping in Figs. 2(b) and 2(f), into selected spectra with position indexes (#1 to #64), as shown in Figs. 2(d) and 2(h), respectively. The spectra #32 and #34 in Fig. 2(d) (colored in blue) are obtained at the blue boundary, while spectra #29 and #32 in Fig. 2(h) (colored in red) are taken at the red boundary. For the blue boundary, the characteristic peak in the CB shifts from 1.24 ± 0.1 to 1.38 ± 0.1 eV, which indicates a 0.14 eV band bending, approaching the boundary. For the red boundary, the band peak in CB shifts from 1.24 ± 0.1 to 1.87 ± 0.1 eV with a 0.63 eV band bending. As marked in the schematic, the band bending results indicate the distinct interfacial charge, induced by different atomic configurations at the blue and red boundaries.

To fabricate the organic-2D heterostructure for improving the band alignment, we deposit the organic acceptor, TCNQ, onto the monolayer PtSe$_2$ with GBs. The molecular structure of TCNQ is shown in the inset of Fig. 3(a). The TCNQ is essentially planar with four cyanide-group at both ends. Figure 3(a) shows the representative STM topography image after the deposition of TCNQ molecules. Obviously, the TCNQ molecules only adsorb at the GBs, forming a stripe structure. Based on the orientation of the moiré pattern, the blue and red boundaries can be recognized and marked. Then we find that all the TCNQ molecules adsorb on the red boundaries, as labeled in Fig. 3(a). In detail, at the red boundaries, the TCNQ molecules always form a single molecule stripe on the UL, while the width of the stripes on the LL varies. The TCNQ stripes always fully occupy the whole adsorbed red boundaries, and leave the blue boundaries empty, although they are very closed to each other.

Furthermore, to investigate the structure of TCNQ stripes, Fig. 3(c) presents the zoomed-in high-resolution STM image of the TCNQ stripe packed as four molecule rows. According to the features of the UL moiré pattern, marked with a red triangle, the position of each TCNQ, about the red boundary, can be roughly achieved. In addition, we can infer the orientation of the TCNQ in different rows, with the combination of the molecular orbital feature in the STM image and the calculated spatial structure of molecular orbitals (highest occupied molecular orbital (HOMO) and lowest unoccupied molecular orbital (LUMO)), shown in Fig. 3(b). Thus, the corresponding configuration model of the TCNQ stripes at the red boundary can be depicted as the schematic shown in Fig. 3(d), with the names labeled. Then, we can see the TCNQ molecules in A and B rows are attached to the boundary edge, which is labeled with the red ribbon in Fig. 3(d).

Next to the structural characterizations, the STS constant-height dI/dV spectra were acquired on the UL, TNCQ molecules in four rows, and LL, as shown in the inset of Fig. 4(a), to investigate the band alignment at GBs covered by TCNQ. As shown in Fig. 4, the
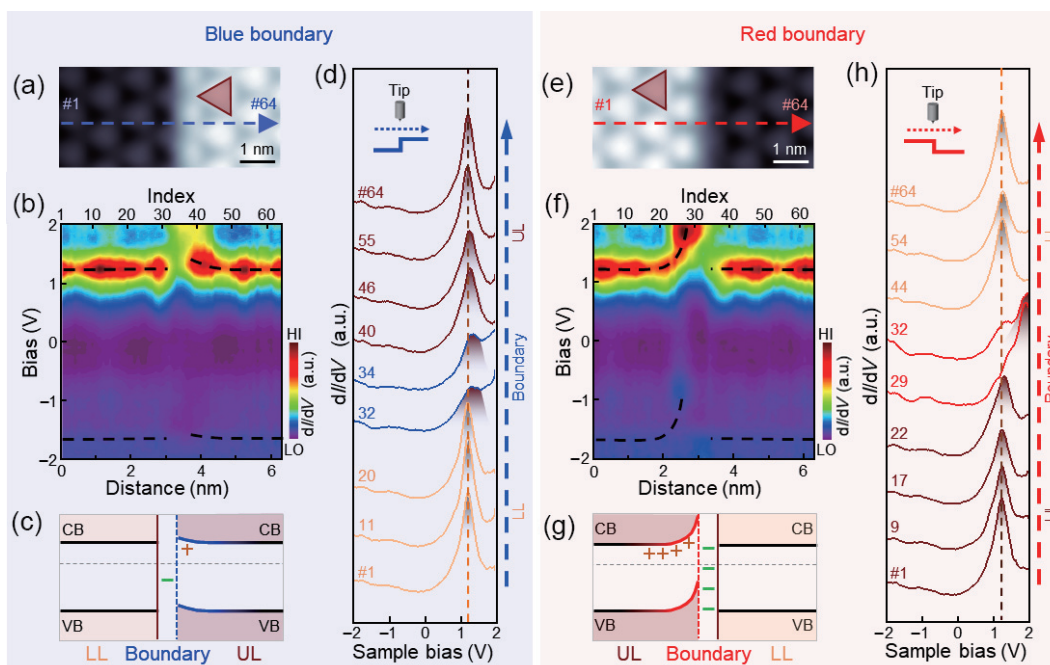

Figure 2 (a) and (e) Topography STM images of the blue (a) and red (e) boundary in monolayer PtSe$_2$. (b) and (f) The constant height dI/dV STS linescans along the blue and red dashed arrows in (a) and (e), respectively. The total length is 6.4 nm with a step size of 0.1 nm. The band bending approaching the boundary is depicted with the black dashed lines. (c) and (g) The schematic diagrams of band alignment at the blue (c) and red (g) boundary. The band bending and accumulated charge are depicted with blue (red) lines and "+/−" signs, respectively. (d) and (h) The subsets of the selected dI/dV spectra with position indexes according to the line profiles in (a) and (e). In (d), spectra #32 and #34 (colored in blue) are obtained at the blue boundary. In (h), spectra #29 and #32 (colored in red) are obtained at the red boundary. STM scanning parameters: ((a) and (e)) $U = -1.0$ V, $I = 50$ pA. The stabilized bias and set-point current for each dI/dV spectrum are $U = -2.0$ V and $I = 50$ pA, respectively.
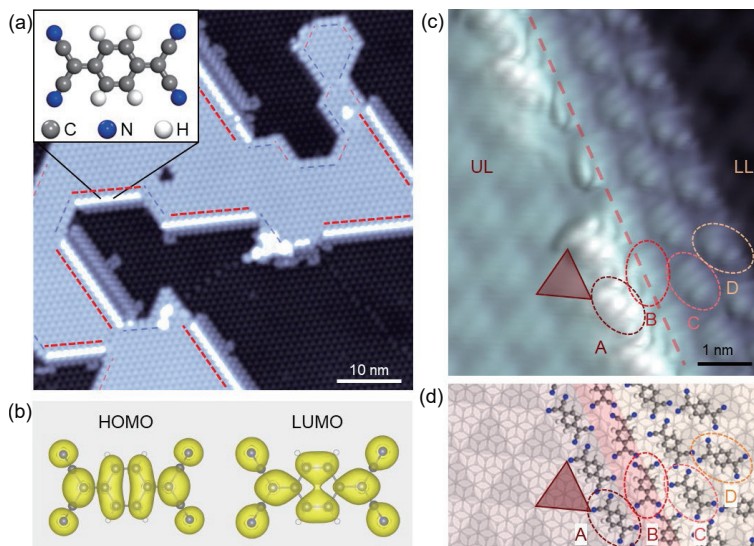
Figure 3 (a) The STM image of TCNQ on monolayer PtSe$_2$ with selective absorption on the red boundary. The grain boundaries are marked with blue and red dashed lines. The grain boundaries with TCNQ absorption are highlighted with thick red dashed lines. (b) Calculated molecular orbitals (HOMO and LUMO) of a single TCNQ molecule. (c) A high-resolution zoom-in STM image of TCNQ molecules adsorbed with different orientations at the red boundary. The position of the boundary is marked with the red dashed line. (d) Schematic of the TCNQ molecular configuration described in (b). The moiré superlattice on UL is depicted by red triangles. The molecules named A, B, C, and D are marked with corresponding dashed circles in (b) and (d). STM scanning parameters: (a) $U = -1.0$ V, $I = 50$ pA; (b) $U = 0.3$ V, $I = 50$ pA.

spectra of LL and UL reveal the characteristic peaks at +1.24 eV in the CB, which are the same as the corresponding results in Figs. 2(d) and 2(g). In the spectra taken on TCNQ molecules (for more details see Fig. S5 in the ESM), we can see double-peaks lay at around +0.5 eV, which are the LUMO states [38]. In detail, the LUMO peaks lay at +0.54, +0.55, +0.51, and +0.44 eV for the molecules in A, B, C, and D rows, respectively. We can see that the TCNQ molecules in A and B rows own shifted LUMO state with higher energy positions, compared with the molecules in C and D rows, which are on the inner. It hints at an additional charge transfer between the boundary edge and the attached molecules in the A and B rows.

Besides the molecular orbital peaks, there is another peak at around +1.24 eV in each spectrum taken on the molecules, as labeled in Fig. 4(a). As reported, the next higher unoccupied orbitals are at 3 eV above the LUMO [38]. Considering the similar energy position, this peak is associated with the direct tunneling

into the characteristic peaks in the PtSe$_2$ CB. Unlike the band bending feature, we can find that the peak positions remain around +1.24 eV at A and B TCNQ rows attached to the boundary, which is the position owning an upward band bending to +1.87 eV without the TCNQ. It indicates that the band bending of the red boundary is almost eliminated by charge transfer with the adsorbed TCNQ. The charge transfer model was schematically illustrated in Figs. 4(b) and 4(c). Without the TCNQ adsorption, there is a distinct interfacial charge generated by the GBs. As an electron acceptor, the TCNQ molecule owns selective adsorption on the red boundary and receives the interfacial charge via the van der Waals interaction from the boundary edge (for more details see Figs. S6 and S7 in the ESM). Consequently, the interfacial charge is neutralized and the corresponding band bending is suppressed.

As illustrated by the schematic diagram shown in Fig. 4(d), limiting the interfacial charge via the interaction with the edge, the
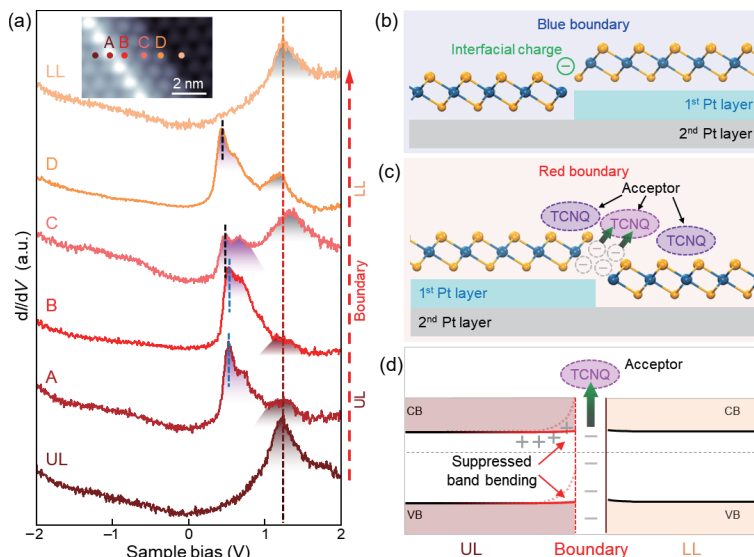

Figure 4 (a) The STS spectra acquired on the TCNQ molecules adsorbed at the red boundary. The positions of each STS spectra are labeled on the STM image in the inset. The peaks are marked with dashed lines. (b) and (c) Schematic of the interfacial charge of blue boundary and red boundary with TCNQ adsorption. (d) Schematic diagram of the band alignment at the red boundary with TCNQ. STM scanning parameters: (a) $U = -1.0$ V, $I = 50$ pA. The stabilized bias and set-point current for each dI/dV spectrum are $U = -2.0$ V and $I = 50$ pA, respectively.

TCNQ adsorbed at the boundary acts more like an introduced defect or impurity, instead of the one side of the GBs. The main contact in the GBs is still between the UL and LL PtSe$_2$. Although redundant TCNQ molecules also have charge transfer with LL PtSe$_2$, the induced band bending is slight, as revealed by the slight peak shift in the spectrum of C row in Fig. 4(a). It indicates that the band bending at GBs can be suppressed by the adsorption of TCNQ, without inducing significant changes in the electronic structure of PtSe$_2$. We can infer that organic-2D heterostructure with site-specific selective adsorption, formed with the organic donors or acceptors, can be used for precisely improving the band alignment at the GBs of 2D semiconductors.

4 Conclusions

In summary, using STM/S measurements, we demonstrate that the band alignment at the GBs of monolayer PtSe$_2$ can be improved by the TCNQ selective adsorption. We fabricated the organic-2D heterostructure with monolayer PtSe$_2$ and TCNQ. Our results reveal that the molecules are preferentially adsorbed at the boundaries, which own stronger band bending and interfacial charge. Due to the interaction between the boundary and the adsorption of TCNQ, the band bending at the GBs can be suppressed, without inducing excessive effects on the PtSe$_2$ electronic structures. Extending the application of organic-2D heterostructures, this work offers a promising method to precisely improve the band alignment at the grain boundaries and weaken their impairing effect on the properties of 2D semiconductors. Thus, it will facilitate the electronic properties of two-dimensional semiconductors for its future applications.

Acknowledgements

Electronic Supplementary Material: Supplementary materia (the model of the ML PtSe$_2$/Pt(111) moiré pattern, the corresponding STM simulation, the STS mapping of the TCNQ on the boundary, and the additional DFT calculation results) is available in the online version of this article at https://doi.org/10.1007/s12274-022-5009-8.

References

[1] Yu, Z. H.; Ong, Z. Y.; Li, S. L.; Xu, J. B.; Zhang, G.; Zhang, Y. W.; Shi, Y.; Wang, X. R. Analyzing the carrier mobility in transition-metal dichalcogenide MoS$_2$ field-effect transistors. *Adv. Funct. Mater.* **2017**, *27*, 1604093.

[2] Cui, C. J.; Xue, F.; Hu, W. J.; Li, L. J. Two-dimensional materials with piezoelectric and ferroelectric functionalities. *npj 2D Mater. Appl.* **2018**, *2*, 18.

[3] Zhang, Y.; Yao, Y. Y.; Sendeku, M. G.; Yin, L.; Zhan, X. Y.; Wang, F.; Wang, Z. X.; He, J. Recent progress in CVD growth of 2D transition metal dichalcogenides and related heterostructures. *Adv. Mater.* **2019**, *31*, 1901694.

[4] Si, M. W.; Saha, A. K.; Gao, S. J.; Qiu, G.; Qin, J. K.; Duan, Y. Q.; Jian, J.; Niu, C.; Wang, H. Y.; Wu, W. Z. et al. A ferroelectric semiconductor field-effect transistor. *Nat. Electron.* **2019**, *2*, 580–586.

[5] Sung, J.; Zhou, Y.; Scuri, G.; Zólyomi, V.; Andersen, T. I.; Yoo, H.; Wild, D. S.; Joe, A. Y.; Gelly, R. J.; Heo, H. et al. Broken mirror symmetry in excitonic response of reconstructed domains in twisted MoSe$_2$/MoSe$_2$ bilayers. *Nat. Mater.* **2020**, *15*, 750–754.

[6] Andersen, T. I.; Scuri, G.; Sushko, A.; De Greve, K.; Sung, J.; Zhou, Y.; Wild, D. S.; Gelly, R. J.; Heo, H.; Bérubé, D. et al. Excitons in a reconstructed moiré potential in twisted WSe$_2$/WSe$_2$ homobilayers. *Nat. Mater.* **2021**, *20*, 480–487.

[7] Reato, E.; Palacios, P.; Uzlu, B.; Saeed, M.; Grundmann, A.; Wang, Z. Y.; Schneider, D. S.; Wang, Z. X.; Heuken, M.; Kalisch, H. et al. Zero-bias power-detector circuits based on MoS$_2$ field-effect transistors on wafer-scale flexible substrates. *Adv. Mater.*, in press, https://doi.org/10.1002/adma.202108469.

[8] Wang, Y.; Chhowalla, M. Making clean electrical contacts on 2D transition metal dichalcogenides. *Nat. Rev. Phys.* **2022**, *4*, 101–112.

[9] Yagodkin, D.; Greben, K.; Eljarrat, A.; Kovalchuk, S.; Ghorbani-Asl, M.; Jain, M.; Kretschmer, S.; Severin, N.; Rabe, J. P.; Krasheninnikov, A. V. et al. Extrinsic localized excitons in patterned 2D semiconductors. *Adv. Funct. Mater.* **2022**, *32*, 2203060.

[10] Van Der Zande, A. M.; Huang, P. Y.; Chenet, D. A.; Berkelbach, T. C.; You, Y. M.; Lee, G. H.; Heinz, T. F.; Reichman, D. R.; Muller, D. A.; Hone, J. C. Grains and grain boundaries in highly crystalline monolayer molybdenum disulphide. *Nat. Mater.* **2013**, *12*, 554–561.

[11] Ly, T. H.; Perello, D. J.; Zhao, J.; Deng, Q. M.; Kim, H.; Han, G. H.; Chae, S. H.; Jeong, H. Y.; Lee, Y. H. Misorientation-angle-dependent electrical transport across molybdenum disulfide grain boundaries. *Nat. Commun.* **2016**, *7*, 10426.

[12] Chen, J.; Jung, G. S.; Ryu, G. H.; Chang, R. J.; Zhou, S.; Wen, Y.; Buehler, M. J.; Warner, J. H. Atomically sharp dual grain boundaries in 2D WS$_2$ bilayers. *Small* **2019**, *15*, 1902590.

[13] Murray, C.; van Efferen, C.; Jolie, W.; Fischer, J. A.; Hall, J.; Rosch, A.; Krasheninnikov, A. V.; Komsa, H. P.; Michely, T. Band bending and valence band quantization at line defects in MoS$_2$. *ACS Nano* **2020**, *14*, 9176–9187.

[14] Gong, Y. J.; Ye, G. L.; Lei, S. D.; Shi, G.; He, Y. M.; Lin, J. H.; Zhang, X.; Vajtai, R.; Pantelides, S. T.; Zhou, W. et al. Synthesis of millimeter-scale transition metal dichalcogenides single crystals. *Adv. Funct. Mater.* **2016**, *26*, 2009–2015.

[15] Chen, S.; Gao, J. F.; Srinivasan, B. M.; Zhang, G.; Yang, M.; Chai, J. W.; Wang, S. J.; Chi, D. Z.; Zhang, Y. W. Revealing the grain boundary formation mechanism and kinetics during polycrystalline MoS$_2$ growth. *ACS Appl. Mater. Interfaces* **2019**, *11*, 46090–46100.

[16] Xu, X. M.; Das, G.; He, X.; Hedhili, M. N.; Di Fabrizio, E.; Zhang, X. X.; Alshareef, H. N. High-performance monolayer MoS$_2$ films at the wafer scale by two-step growth. *Adv. Funct. Mater.* **2019**, *29*, 1901070.

[17] Huang, Y.; Yu, K.; Li, H. Z.; Xu, K.; Liang, Z. X.; Walker, D.; Ferreira, P.; Fischer, P.; Fan, D. L. Scalable fabrication of molybdenum disulfide nanostructures and their assembly. *Adv. Mater.* **2020**, *32*, 2003439.

[18] Zhang, W. F.; Zhang, Y.; Qiu, J. K.; Zhao, Z. H.; Liu, N. Topological structures of transition metal dichalcogenides: A review on fabrication, effects, applications, and potential. *InfoMat* **2021**, *3*, 133–154.

[19] Yu, X. T.; Wang, X.; Zhou, F. F.; Qu, J. L.; Song, J. 2D van der Waals heterojunction nanophotonic devices: From fabrication to performance. *Adv. Funct. Mater.* **2021**, *31*, 2104260.

[20] Huang, Y. L.; Chen, Y. F.; Zhang, W. J.; Quek, S. Y.; Chen, C. H.; Li, L. J.; Hsu, W. T.; Chang, W. H.; Zheng, Y. J.; Chen, W. et al. Bandgap tunability at single-layer molybdenum disulphide grain boundaries. *Nat. Commun.* **2015**, *6*, 6298.

[21] Barja, S.; Wickenburg, S.; Liu, Z. F.; Zhang, Y.; Ryu, H.; Ugeda, M. M.; Hussain, Z.; Shen, Z. X.; Mo, S. K.; Wong, E. et al. Charge density wave order in 1D mirror twin boundaries of single-layer MoSe$_2$. *Nat. Phys.* **2016**, *12*, 751–756.

[22] Wang, L.; Wu, Y.; Yu, Y. Y.; Chen, A. X.; Li, H. F.; Ren, W.; Lu, S.; Ding, S. A.; Yang, H.; Xue, Q. K. et al. Direct observation of one-dimensional Peierls-type charge density wave in twin boundaries of monolayer MoTe$_2$. *ACS Nano* **2020**, *14*, 8299–8306.

[23] Yao, W. Q.; Wu, B.; Liu, Y. Q. Growth and grain boundaries in 2D materials. *ACS Nano* **2020**, *14*, 9320–9346.

[24] Zhang, Q. Z.; Hou, Y. H.; Zhang, T.; Xu, Z. Q.; Huang, Z. P.; Yuan, P. W.; Jia, L. G.; Yang, H. X.; Huang, Y.; Ji, W. et al. Visualizing spatial evolution of electron−correlated interface in two-dimensional heterostructures. *ACS Nano* **2021**, *15*, 16589–16596.

[25] Liu, F. C.; Chow, W. L.; He, X. X.; Hu, P.; Zheng, S. J.; Wang, X. L.; Zhou, J. D.; Fu, Q. D.; Fu, W.; Yu, P. et al. Van der Waals p-n junction based on an organic−inorganic heterostructure. *Adv. Funct. Mater.* **2015**, *25*, 5865–5871.

[26] Huang, Y. L.; Zheng, Y. J.; Song, Z. B.; Chi, D. Z.; Wee, A. T. S.; Quek, S. Y. The organic-2D transition metal dichalcogenide heterointerface. *Chem. Soc. Rev.* **2018**, *47*, 3241–3264.

[27] Sun, J.; Choi, Y.; Choi, Y. J.; Kim, S.; Park, J. H.; Lee, S.; Cho, J. H. 2D-organic hybrid heterostructures for optoelectronic applications. *Adv. Mater.* **2019**, *31*, 1803831.

[28] Ulman, K.; Quek, S. Y. Organic-2D material heterostructures: A promising platform for exciton condensation and multiplication. *Nano Lett.* **2021**, *21*, 8888–8894.

[29] Lin, X.; Lu, J. C.; Shao, Y.; Zhang, Y. Y.; Wu, X.; Pan, J. B.; Gao, L.; Zhu, S. Y.; Qian, K.; Zhang, Y. F. et al. Intrinsically patterned two-dimensional materials for selective adsorption of molecules and nanoclusters. *Nat. Mater.* **2017**, *16*, 717–721.

[30] He, X. Y.; Zhang, L.; Chua, R.; Wong, P. K. J.; Arramel, A.; Feng, Y. P.; Wang, S. J.; Chi, D. Z.; Yang, M.; Huang, Y. L. et al. Selective self-assembly of 2, 3-diaminophenazine molecules on MoSe₂ mirror twin boundaries. *Nat. Commun.* **2019**, *10*, 2847.

[31] Park, J. H.; Sanne, A.; Guo, Y. Z.; Amani, M.; Zhang, K. H.; Movva, H. C. P.; Robinson, J. A.; Javey, A.; Robertson, J.; Banerjee, S. K. et al. Defect passivation of transition metal dichalcogenides via a charge transfer van der Waals interface. *Sci. Adv.* **2017**, *3*, e1701661.

[32] Wang, Y. L.; Li, L. F.; Yao, W.; Song, S. R.; Sun, J. T.; Pan, J. B.; Ren, X.; Li, C.; Okunishi, E.; Wang, Y. Q. et al. Monolayer PtSe₂, a new semiconducting transition-metal-dichalcogenide, epitaxially grown by direct selenization of Pt. *Nano Lett.* **2015**, *15*, 4013–4018.

[33] Zhao, Y. D.; Qiao, J. S.; Yu, Z. H.; Yu, P.; Xu, K.; Lau, S. P.; Zhou, W.; Liu, Z.; Wang, X. R.; Ji, W. et al. High-electron-mobility and air-stable 2D layered PtSe₂ FETs. *Adv. Mater.* **2017**, *29*, 1604230.

[34] Yao, W.; Wang, E. Y.; Huang, H. Q.; Deng, K.; Yan, M. Z.; Zhang, K. N.; Miyamoto, K.; Okuda, T.; Li, L. F.; Wang, Y. L. et al. Direct observation of spin-layer locking by local Rashba effect in monolayer semiconducting PtSe₂ film. *Nat. Commun.* **2017**, *8*, 14216.

[35] Xu, H.; Zhang, H. M.; Liu, Y. W.; Zhang, S. M.; Sun, Y. Y.; Guo, Z. X.; Sheng, Y. C.; Wang, X. D.; Luo, C.; Wu, X. et al. Controlled doping of wafer-scale PtSe₂ films for device application. *Adv. Funct. Mater.* **2019**, *29*, 1805614.

[36] Wu, X.; Qiao, J. S.; Liu, L. W.; Shao, Y.; Liu, Z. L.; Li, L. F.; Zhu, Z. L.; Wang, C.; Hu, Z. X.; Ji, W. et al. Shallowing interfacial carrier trap in transition metal dichalcogenide heterostructures with interlayer hybridization. *Nano Res.* **2021**, *14*, 1390–1396.

[37] Li, J. F.; Joseph, T.; Ghorbani-Asl, M.; Kolekar, S.; Krasheninnikov, A. V.; Batzill, M. Edge and point-defect induced electronic and magnetic properties in monolayer PtSe₂. *Adv. Funct. Mater.* **2022**, *32*, 2110428.

[38] Yousofnejad, A.; Reecht, G.; Krane, N.; Lotze, C.; Franke, K. J. Monolayers of MoS₂ on Ag(111) as decoupling layers for organic molecules: Resolution of electronic and vibronic states of TCNQ. *Beilstein J. Nanotechnol.* **2020**, *11*, 1062–1071.